Analysis and Calculation of Current Ripple Considering Inductance Saturation and Its Application to Variable Switching Frequency PWM

Qiao Li, *Student Member, IEEE*, Dong Jiang, *Senior Member, IEEE*, and Yechi Zhang, *Student Member, IEEE*

***Abstract*—The inductance is an important parameter impacting current ripple calculation, usually with the assumption that the designed inductance performs ideally in most of voltage source inverters (VSIs) applications. However, the initial permeability of magnetic material usually descends when the winding current reaches or goes beyond the saturation limit. In such region of saturation, the implemented inductor does not perform as expected in design stages and its value varies with the bias current. In this paper, analysis and calculation of the current ripple are presented for a three-phase VSI with powder cores-based inductors, which reveals the calculation error of current ripple caused by the soft saturation nature of powder cores. Based on the equivalent single-phase model, the influence of inductance saturation on current ripple can be quantitatively evaluated. Then, a comparison of the current ripple calculation between considering and ignoring inductance saturation of implemented inductors is drawn in detail. Furthermore, under the condition of inductance saturation, the output current ripple peak-to-peak value of three phases is used as the constraint for variable switching frequency pulsewidth modulation (VSFPWM) design. A comprehensive method is developed to compensate the effect of inductance saturation in VSFPWM. At last, the effectiveness of the proposed strategy is verified by the detailed simulation and experiment.**

***Index Terms*—Current ripple, electromagnetic interference (EMI), inductance saturation, variable switching frequency pulsewidth modulation (VSFPWM).**

I. Introduction

VOLTAGE source inverters (VSIs) have been widely used in motor drives, uninterruptible power supplies, and renewable energy generation, etc. In most of VSIs applications, pulsewidth modulation (PWM) schemes are commonly employed for energy conversion, and are mainly divided into space vector PWM (SVPWM) and carrier-based PWM (CBPWM). In fact, the CBPWM is equivalent to the SVPWM, by the way of zero-sequence modulating signal injection [1], [2]. Following

Manuscript received November 12, 2018; revised January 14, 2019; accepted March 2, 2019. Date of publication March 8, 2019; date of current version September 6, 2019. This work was supported in part by the National Natural Science Foundation of China under Grant 51607077 and in part by the State Grid of China Project under Grant SGTYHT/16-JS-198. Recommended for publication by Associate Editor J. Liu. *(Corresponding author: Dong Jiang.)*

The authors are with the State Key Laboratory of Advanced Electromagnetic Engineering and Technology, School of Electrical and Electronic Engineering, Huazhong University of Science and Technology, Wuhan 430074, China (e-mail:

calculation with consideration of the soft-saturation nature of the powder cores.

Variable switching frequency PWM (VSFPWM) based on the current ripple prediction is developed in recent years. As discussed in [18] and [19], the peak-to-peak or rms value of current ripple in each switching cycle varies along with the position of voltage vector and modulation index, within a fundamental period. A freedom of switching frequency is utilized to control the current ripple distribution for switching losses reduction and EMI improvement, but still remaining the current distortion within the limit. Different from the model predictive control [20]–[22], VSFPWM is still based on the conventional feedback control, where PWM module still exists in the system. Comparing with the conventional constant switching frequency PWM (CSFPWM), VSFPWM can utilize a freedom of switching frequency to improve the system performance.

However, in previous literatures, the current ripple calculation model is well used in traditional VSFPWM (T-VSFPWM) with the assumption that the designed inductance performs ideally in hardware applications, in which there is hardly any consideration of the effect of inductance saturation. In fact, inductance variation caused by core saturation is a very common phenomenon in VSI applications. If the T-VSFPWM is directly implemented in a VSI system using inductors characterized by inductance variation, current ripple prediction cannot match well in many cases and the control error of current ripple can be easily introduced. To overcome this issue of T-VSFPWM, a modified VSFPWM (M-VSFPWM) is proposed in this paper to use VSF technique under the condition of inductance saturation, while maintaining the current ripple constraint at the same level in CSFPWM.

The rest of this paper is organized as follows. In Section II, the introduction of an artificial inductance and common-mode (CM) voltage is presented. Then, the definition of output current ripple considering inductance saturation is derived and a general single-phase calculation model of current ripple is proposed. Using this model, the current ripple can be accurately predicted under the condition of inductance variation. Furthermore, an M-VSFPWM strategy is proposed in Section III. Cases reflecting the influence of inductance saturation on current calculation and the investigation in CSFPWM, T-VSFPWM, and the proposed M-VSFPWM are shown in Section IV through the MATLAB/Simulink. Experiments are carried out on a two-level three-phase VSI system using digital signal processor (DSP) control board in Section V. Finally, useful conclusions are summarized in Section VI.

II. Current Ripple Analysis Considering Inductance Saturation

The topology of a two-level three-phase VSI system is presented in Fig. 1, where three-phase inductors are inserted in the ac-side. Two line impedance stabilization networks are used here to prevent external conductive noise from the dc source, and *electromagnetic interference* (EMI) transmission paths are also depicted in Fig. 1, where CM and differential-mode EMI are two forms of conducted EMI. Note that the inductance of line inductor varies over a wide range when ac current changes in a period.

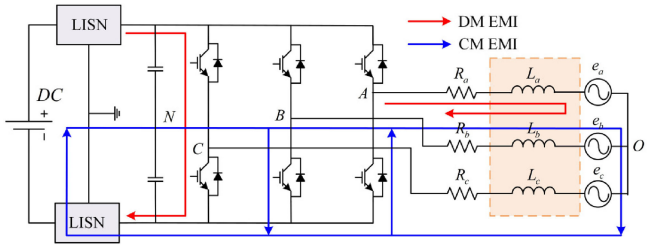

Fig. 1. Equivalent circuit for a two-level VSI.

A. Introduction of an Artificial Inductance and CM Voltage

Observed from Fig. 1, the inductance variation is taken into account. V_{KN} $(K = A, B, C)$ is the terminal voltage of three phases with reference to dc link mid-point *N*, L_k $(k = a, b, c)$ is the line inductance, R_k is the series resistance, and $V_{\rm ON}$ is defined as the CM voltage. According to the Kirchhoff voltage law, the voltage equation is written for three phases as

$$\begin{cases} V_{AN}(t) - V_{ON}(t) = Ri_a(t) + \dfrac{d\psi_a}{dt} + e_a(t) \\ V_{BN}(t) - V_{ON}(t) = Ri_b(t) + \dfrac{d\psi_b}{dt} + e_b(t) \\ V_{CN}(t) - V_{ON}(t) = Ri_c(t) + \dfrac{d\psi_c}{dt} + e_c(t) \end{cases} \tag{1}$$

where Ψ_k stands for the excitation flux linkage in the line inductor, and the second term on the right side accounts for the inductance voltage drop of ac current, which can be expressed as

$$\begin{cases} \dfrac{d\psi_a}{dt} = L_a\dfrac{di_a}{dt} + i_a\dfrac{dL_a}{di_a}\dfrac{di_a}{dt} = \left(L_a + i_a\dfrac{dL_a}{di_a}\right)\dfrac{di_a}{dt} \\ \dfrac{d\psi_b}{dt} = L_b\dfrac{di_b}{dt} + i_b\dfrac{dL_b}{di_b}\dfrac{di_b}{dt} = \left(L_b + i_b\dfrac{dL_b}{di_b}\right)\dfrac{di_b}{dt} \\ \dfrac{d\psi_c}{dt} = L_c\dfrac{di_c}{dt} + i_c\dfrac{dL_c}{di_c}\dfrac{di_c}{dt} = \left(L_c + i_c\dfrac{dL_c}{di_c}\right)\dfrac{di_c}{dt}. \end{cases} \tag{2}$$

Generally, the inductance L_k is considered to be a constant value, which means that variation of the inductance with the bias current can be ignored, and $i_k dL_k/di_k$ is always kept to be zero. In practice, the inductance L_k will decrease when ac current reaches or goes beyond the saturation limit of the line inductor. Having this fact in mind, an artificial inductance L_k^* can be defined as

$$L_k^* = L_k + i_k\frac{dL_k}{di_k}. \tag{3}$$

Equation (3) describes how the inductance variation is introduced under ac current flow. The following can be observed.

1) L_k^* is the artificial inductance for phase-*k* and it consists of two terms. The first term L_k is the effective inductance, which is a function of permeability of the magnetic core related to the bias current through the inductor; the second term $i_k dL_k/di_k$ stands for the product of the bias current and the derivative of inductance to bias current.

2) Once the effective inductance is not a constant value, the variation of effective inductance and the bias current, which are involved in the artificial inductance, will then influence the current ripple analysis.
3) L_k^* is still a function of bias current through the inductor. Both the two terms change along with bias current and it is worth noting that L_k^* is just determined by the bias current if the saturation characteristic of the inductor has been designed.

Substituting (2) and (3) into (1), the following equations are then obtained:

$$\begin{cases} [V_{AN}(t)-V_{\rm ON}(t)]\,L_b^*L_c^*=\left[Ri_a(t)+L_a^*\dfrac{di_a}{dt}+e_a(t)\right]L_b^*L_c^* \\ [V_{BN}(t)-V_{\rm ON}(t)]\,L_a^*L_c^*=\left[Ri_b(t)+L_b^*\dfrac{di_b}{dt}+e_b(t)\right]L_a^*L_c^* \\ [V_{CN}(t)-V_{\rm ON}(t)]\,L_a^*L_b^*=\left[Ri_c(t)+L_c^*\dfrac{di_c}{dt}+e_c(t)\right]L_a^*L_b^*. \end{cases} \tag{4}$$

Ignoring the resistance voltage drop and adding (4), the instantaneous CM voltage can be deduced as

$$V_{\rm ON}(t)=\frac{L_b^*L_c^*V_{AN}(t)+L_a^*L_c^*V_{BN}(t)+L_a^*L_b^*V_{CN}(t)}{L_b^*L_c^*+L_a^*L_c^*+L_a^*L_b^*} - \frac{L_b^*L_c^*e_a(t)+L_a^*L_c^*e_b(t)+L_a^*L_b^*e_c(t)}{L_b^*L_c^*+L_a^*L_c^*+L_a^*L_b^*}. \tag{5}$$

Considering the inductance saturation characteristics, the values of L_a^*, L_b^*, and L_c^* are different because three-phase ac current differ, and the practical CM voltage is a function of three-phase artificial inductance, terminal voltage, and load voltage. Specially, it may be observed from (5) that the CM voltage can be simplified as $[V_{AN}(t)+V_{BN}(t)+V_{CN}(t)]/3$ if the artificial inductance is regarded as an unsaturated value. Therefore, the normal CM voltage definition of a three-phase VSI is just a special case, in which artificial inductance is treated to be a constant value.

B. Definition of Output Current Ripple

Due to the symmetry of three-phase VSI, phase-*a* is studied for current ripple analysis, taking into account the inductance variation. Without losing generality, averaging (1) for phase-*a* over a switching period T_s leads to

$$\overline{V_{AN}}(T_s)-\overline{V_{\rm ON}}(T_s)=R\overline{i_a}(T_s)+L_a^*\frac{\Delta i_a}{T_s}+\overline{e_a}(T_s) \tag{6}$$

where $\overline{V_{AN}}(T_s)$, $\overline{V_{\rm ON}}(T_s)$, $\overline{i_a}(T_s)$, and $\overline{e_a}(T_s)$ are the average value of $V_{AN}(t)$, $V_{\rm ON}(t)$, $i_a(t)$, and $e_a(t)$ over a switching period, respectively. Δi_a represents the current change of phase-*a* over a switching period. Substituting (2) and (3) into (1), and minus (6), we get

$$\tilde{v}_a(t)=R\left[i_a(t)-\overline{i_a}(T_s)\right]+L_a^*\left[\frac{di_a}{dt}-\frac{\Delta i_a}{T_s}\right] + [e_a(t)-\overline{e_a}(T_s)] \tag{7}$$

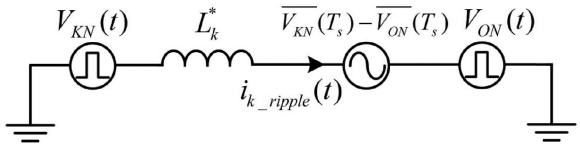

Fig. 2. General single-phase model for current ripple calculation.

where $\tilde{v}_a(t)$ is defined as the difference between instantaneous $v_a(t)$ and average voltage $\bar{v}_a(T_s)$

$$\tilde{v}_a(t)=v_a(t)-\bar{v}_a(T_s) =[V_{AN}(t)-V_{ON}(t)]-\left[\overline{V_{AN}}(T_s)-\overline{V_{ON}}(T_s)\right]. \tag{8}$$

In (7), the first term on the right side accounts for the resistance voltage drop of current ripple and the third term is the deviation between the actual load voltage and its average voltage over one switching period, both of them can be negligible [12]. Thus, it can be simplified as

$$\tilde{v}_a(t)\cong L_a^*\left[\frac{di_a}{dt}-\frac{\Delta i_a}{T_s}\right]. \tag{9}$$

By integrating (9) in sub-period with $t\in[0,T_s]$, the instantaneous current ripple can be defined as

$$i_{a\_\rm ripple}(t)=i_a(t)-\frac{t\Delta i_a}{T_s}\cong\frac{1}{L_a^*}\int_0^t\tilde{v}_a(t)dt \tag{10}$$

where $i_a(t)$ is the full current of phase-*a* and $t\Delta i_a/T_s$ stands for the fundamental current change with time in one switching period.

C. General Single-Phase Model for Current Ripple Calculation

From the aforementioned equations, a general single-phase model for current ripple calculation considering inductance saturation can be deduced as shown in Fig. 2. Focusing on this model, L_k^* and $V_{\rm ON}(t)$ are the artificial inductance and CM voltage, respectively, which have been discussed in Section II-A. $V_{KN}(t)$ is the terminal voltage of phase-*k*, switching between the positive and negative dc-link voltage. $\overline{V_{KN}}(T_s)$ is the average value of terminal voltage of phase-*k* ($k=a,b,c$), which is a constant value over one switching period by regular sampling. $\overline{V_{\rm ON}}(T_s)$ is the average value of instantaneous CM voltage over one switching period. If these parameters are determined for a certain period, the slope of phase-*k* current ripple is

$$\frac{di_{k\_\rm ripple}}{dt}=\frac{1}{L_k^*}\left[V_{KN}(t)-V_{\rm ON}(t)-\overline{V_{KN}}(T_s)+\overline{V_{\rm ON}}(T_s)\right]. \tag{11}$$

As shown in Fig. 3, for a three-phase VSI, the vector space consists of six active vectors (V_1–V_6) and two zero vectors (V_0 and V_7). "1" denotes that the terminal voltage is switched to $V_{\rm dc}/2$ respecting to the dc-link middle point. "0" indicates the output voltage is $-V_{\rm dc}/2$. The vector space is divided into six sectors by six active vectors. Without losing generality, the current ripple analysis can be restricted to the sector I with normal SVPWM. With respect to $V_{\rm ref}$ position, which is located

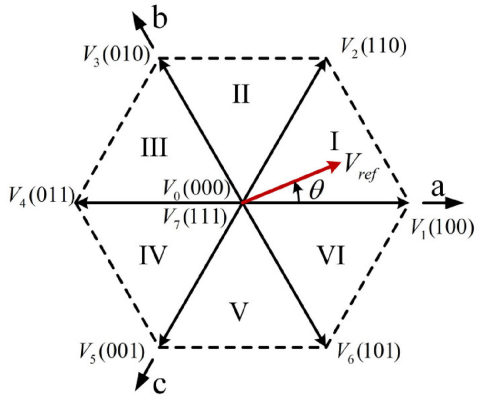

Fig. 3. Space vector diagram.

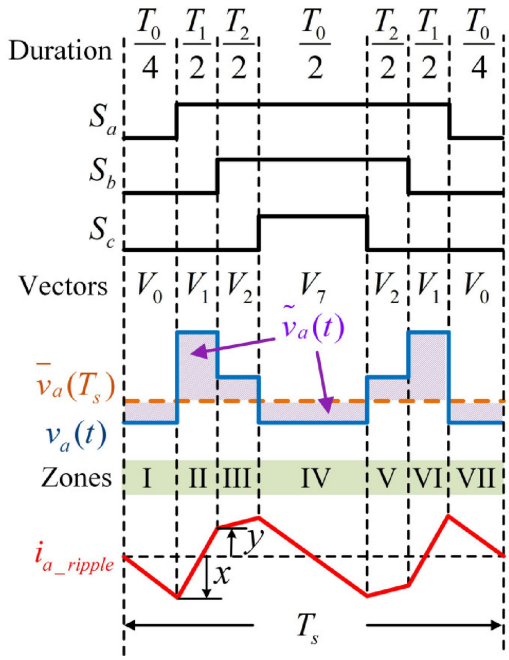

Fig. 4. Current ripple of phase-*a* in one switching cycle with SVPWM.

in sector I, two active vectors (V_1, V_2) and zero vectors (V_0, V_7) are applied to the two-level three-phase VSI. The duration of corresponding vectors T_1, T_2, and T_0 are respectively given in (12), over the switching period T_s.

$$\begin{cases} T_1 = \dfrac{\sqrt{3}}{2} m T_s \sin(\pi/3 - \theta) \\ T_2 = \dfrac{\sqrt{3}}{2} m T_s \sin(\theta) \\ T_0 = T_s - T_1 - T_2 \end{cases} \tag{12}$$

where m is the modulation index and $m = 2|V_{\text{ref}}|/V_{\text{dc}}$. θ is the rotating angle of V_{ref} with respect to the vector V_1, and V_{dc} is the dc-link voltage.

Generally, adjacent active vectors and zero vectors are symmetrically-arranged in each switching period for the normal SVPWM. Fig. 4 shows the switching pulse pattern of three-phase VSI in SVPWM technique, when V_{ref} is located in sector I. The power switches are considered as ideal switches and the dead time is ignored. S_a, S_b, S_c are the switching states, where high-voltage level indicates the upper switch is ON and the lower switch in the same arm is OFF, and vice versa. It can be seen that a sequence of V_0–V_1–V_2–V_7–V_2–V_1–V_0 is used with duration of these seven vectors (T_0/4–T_1/2–T_2/2–T_0/2–T_1/2–T_2/2–T_0/4). With normal SVPWM, there are seven zones corresponding to seven voltage vectors in one switching period. Within each zone, terminal voltage $V_{KN}(t)$ and instantaneous CM voltage $V_{\text{ON}}(t)$ can be obtained and treated as constant. In addition, over one switching period, the average value of three-phase terminal voltage and instantaneous CM voltage can be calculated as follows:

$$\begin{cases} \overline{V_{AN}}(T_s) = \dfrac{V_{\text{dc}}(T_1 + T_2)}{2T_s} \\ \overline{V_{BN}}(T_s) = \dfrac{V_{\text{dc}}(T_2 - T_1)}{2T_s} \\ \overline{V_{CN}}(T_s) = \dfrac{-V_{\text{dc}}(T_1 + T_2)}{2T_s} \end{cases} \tag{13}$$

$$\begin{aligned} &\overline{V_{\text{ON}}}(T_s) \\ &= \frac{L_b^* L_c^* V_{AN}(T_1) + L_a^* L_c^* V_{BN}(T_1) + L_a^* L_b^* V_{CN}(T_1)}{L_b^* L_c^* + L_a^* L_c^* + L_a^* L_b^*} \frac{T_1}{T_s} \\ &+ \frac{L_b^* L_c^* V_{AN}(T_2) + L_a^* L_c^* V_{BN}(T_2) + L_a^* L_b^* V_{CN}(T_2)}{L_b^* L_c^* + L_a^* L_c^* + L_a^* L_b^*} \frac{T_2}{T_s} \\ &- \frac{L_b^* L_c^* \overline{e_a}(T_s) + L_a^* L_c^* \overline{e_b}(T_s) + L_a^* L_b^* \overline{e_c}(T_s)}{L_b^* L_c^* + L_a^* L_c^* + L_a^* L_b^*} \end{aligned} \tag{14}$$

where $V_{KN}(T_1)$ ($K = A$, B, and C) is the terminal voltage of phase-*k* in vector V_1, and $V_{KN}(T_2)$ is the terminal voltage of phase-*k* in vector V_2. $\overline{e_k}(T_s)$ represents the average value of three-phase load voltage over one switching period and the deviation of $\overline{e_k}(T_s)$ from $e_k(t)$ can be negligible. Thus, the last term in (5) and (14) can be considered equal, and canceled each other in (11) for current ripple calculation. It means that no additional load voltage sensors are necessary for current ripple calculation.

In each of the zones, $\tilde{v}_k(t)(k = a, b, c)$ is a constant value, which can be calculated from (5) and (12)–(14), thus the slope of current ripple can be determined by (11) if artificial inductance L_k^* is available. To simplify the analysis L_k^* can be seen as a constant value in one switching period when the fundamental frequency is much lower than the switching frequency. Note that L_k^* needs to be updated cycle by cycle, varying with the bias current. On the other hand, the duration of each zone can be easily achieved from (12). Combining the lope of current ripple and duration in each zone, current ripple of phase-*a* in one switching cycle can be achieved, which is linear in each zone, as shown in Fig. 4. Current ripples of both phase-*b* and phase-*c* can also be obtained. Since the current ripple is symmetrical with respect to the midpoint in each switching cycle for normal SVPWM, the calculation can be simplified for just half switching cycle. Moreover, for each switching cycle, the peak-to-peak $R_{\text{pp\_}a}$ and

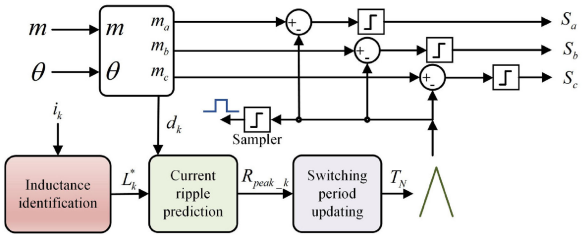

Fig. 5. M-VSFPWM control diagram.

rms value R_{rms_a} of current ripple can also be obtained

$$\begin{cases} R_{\mathrm{pp}\_a} = 2 \times \max\{|x|, |y|\} \\ R_{\mathrm{rms}\_a} = \sqrt{\dfrac{T_0}{T_s}\dfrac{x^2}{3} + \dfrac{T_1+T_2}{T_s}\dfrac{x^2+xy+y^2}{3}}. \end{cases} \tag{15}$$

Although the aforementioned analysis of current ripple is based on the two-level three-phase VSI with SVPWM technique, the proposed general single-phase model for current ripple calculation is also valid to be used for multi-phase or multi-level VSI with other modulation schemes, which are not shown here.

III. Proposed M-VSFPWM

The current ripple prediction is an important basis for VSF-PWM design [18], where the current ripple is calculated in advance and a new switching frequency is generated for certain ripple requirement. For T-VSFPWM [13], [14], constant inductance is utilized for current ripple prediction, thus significant error will be introduced if inductance saturation cannot be ignored. In view of this issue of T-VSFPWM, M-VSFPWM is proposed for current ripple control with the consideration of inductance variation, as shown in Fig. 5. In each switching cycle, three-phase ac currents are obtained from the controller to confirm the artificial inductance $(L_a^*,\ L_b^*,\ L_c^*)$ in the inductance identification module, and then delivered to the current ripple prediction module together with duty cycles $(d_a,\ d_b,\ d_c)$. Based on the current ripple calculation method discussed in Section II, the locus of three-phase current ripple can be predicted. In the switching period updating module, a desired switching period is produced by controlling the peak-to-peak value of three-phase current ripple equal to the requirement according to (16). When the newly triangular carriers are completed, the sampling signal occurs again and next cycle is coming. As a result, the switching frequency is changing cycle by cycle to control the peak-to-peak value of three-phase current ripple equal to the requirement.

$$T_N = T_s \frac{R_{\mathrm{require}}}{\max(|R_{\mathrm{pp}\_k}|)} \tag{16}$$

where T_N is the updated switching period, R_{pp_k} is the predicted peak-to-peak value of phase-k current ripple, and R_{require} stands for the maximum value of three-phase current ripple in a fundamental period for CSFPWM. In this paper, the requirement of current ripple peak-to-peak value is 3 A.

The flowchart of proposed M-VSFPWM in each switching cycle is presented in Fig. 6. Due to the symmetry of current

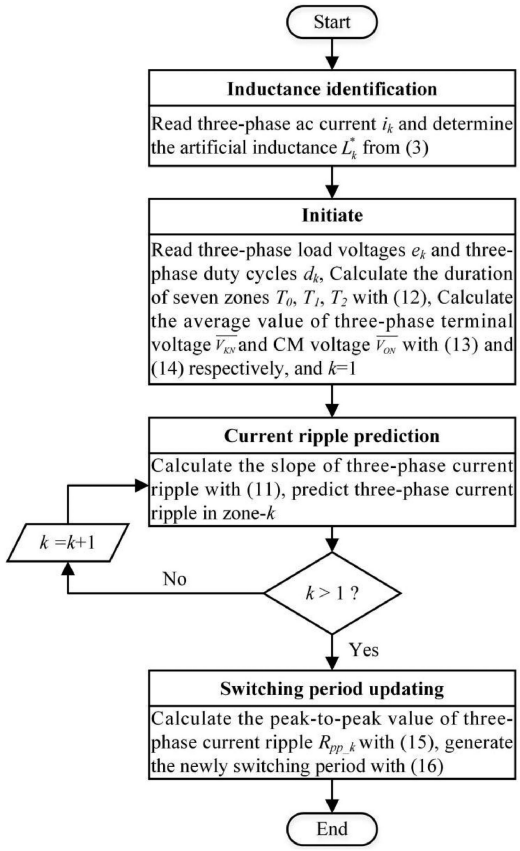

Fig. 6. Flowchart of proposed M-VSFPWM in each switching cycle.

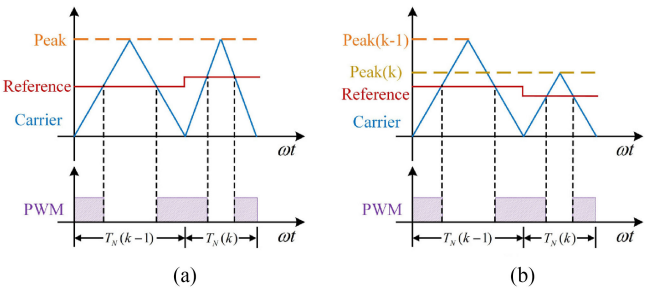

Fig. 7. Carrier wave generator. (a) Varying the counter slope with the constant peak value. (b) Varying the peak value with the constant counter slope.

ripple in one switching cycle, only the first and second zone need to be calculated. In the inductance identification module, three-phase currents (i_k) are needed to determine the artificial inductance in each switching cycle. Thus, three-phase current sensors are necessary for the proposed M-VSFPWM control. Fig. 7 shows the update method of the switching period, where the triangular carrier wave is adopted with an up/down counter. As shown in Fig. 7(a), the peak value of the carrier wave is always set as a constant, and the counter slope is varied cycle by cycle to change the carrier/switching period. On the other hand, the peak value of the carrier wave can be varied cycle by cycle if the counter slope is always programmed as a constant, as shown in Fig. 7(b). It is worth noting that the reference compared with the triangular carrier should be in proportion to the peak value of the carrier wave to ensure volt-second balance. In the

TABLE I
SYSTEM PARAMETERS

Parameters	Value	p.u. value
Rated phase voltage amplitude (E_b)	100 V	1
Rated Capacity (S_b)	3 kVA	1
dc-link voltage (V_{dc})	200 V	1
Phase current amplitude (i)	13.44 A	0.672
Modulation index (m)	0.7	0.7
Load resistance (R)	5 Ω	1
ac-side filter capacitance (C)	35 μF	18.12
ac-side unbiased value of inductance (L)	720 μH	0.0452
Constant switching frequency (f_c)	15 kHz	1

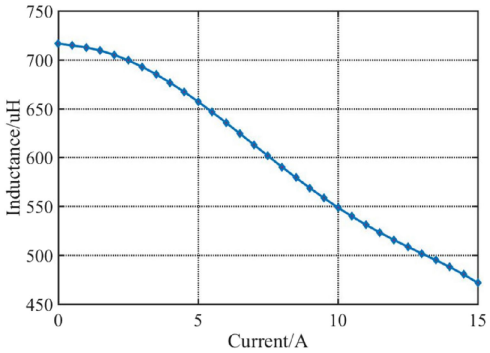

Fig. 8. Effective inductance variation with bias current.

DSP-based system, it is more convenient and efficient to change the peak value (period register) of the carrier wave.

IV. SIMULATION VERIFICATION

The validity of current ripple analysis and proposed M-VSFPWM has been verified through dynamic simulations of a three-phase VSI feeding into *L-C-R* load in MATLAB/Simulink, with the main parameters summarized in Table I. A model of nonlinear inductor has been used here, which is determined by the current vector and magnetic flux vector, using smooth interpolation method.

A. Influence of Inductance Variation on CM Voltage and Current Ripple

Fig. 8 shows the measured inductance variation with bias current, where the effective inductance of line inductor is about 720 μH under low injected current and drops to 500 μH around the current peak (14 A). As it may be observed from Fig. 9 that under the sinusoidal current flow, high bias current will cause the inductance to decrease and a significant difference $(i_a dL_a/di_a)$ between the effective inductance (L_a) and the artificial inductance (L_a^*) can be observed, which is not considered in [17]. It can be seen that the maximum inductance error caused by $i_a dL_a/di_a$ is more than 27%. As can be seen from Fig. 10, the practical CM voltage is not equal to $[V_{AN}(t) + V_{BN}(t) + V_{CN}(t)]/3$ in some zones because of the inductance variation, but matches well with the predicted results proposed in this paper.

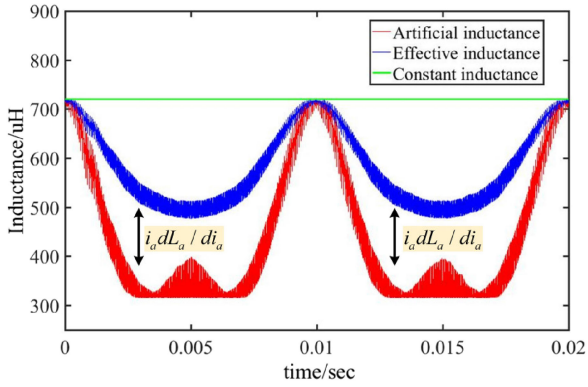

Fig. 9. Inductance variation under sinusoidal current flow.

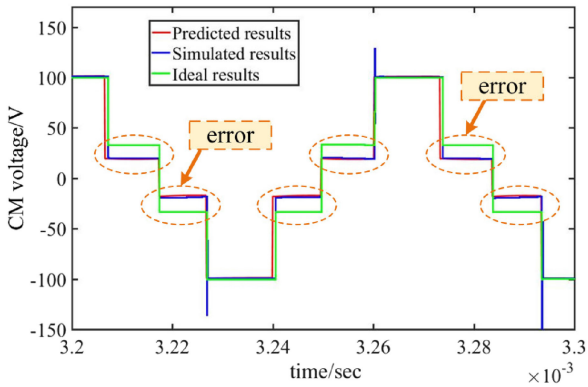

Fig. 10. CM voltage comparison.

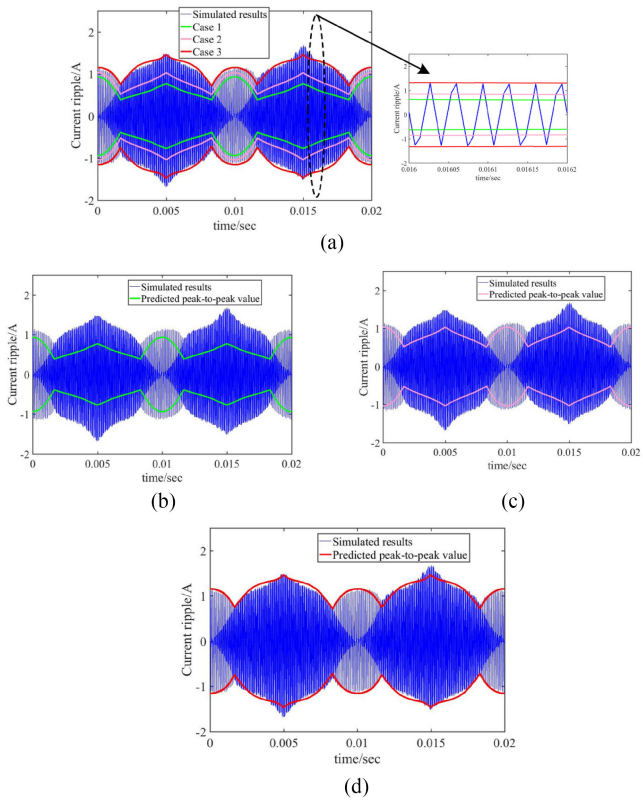

Fig. 11. Simulation results: current ripple comparison of phase-*a*. (a) General plot. (b) Case 1. (c) Case 2. (d) Case 3.

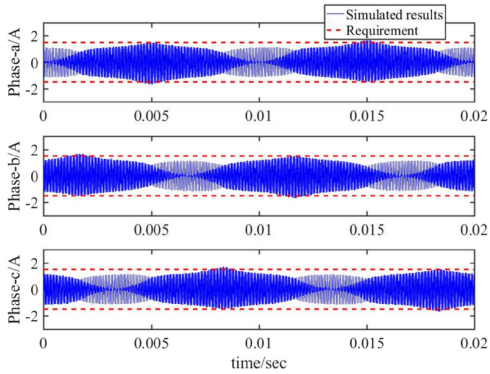

Fig. 12. Current ripple of three phases with CSFPWM.

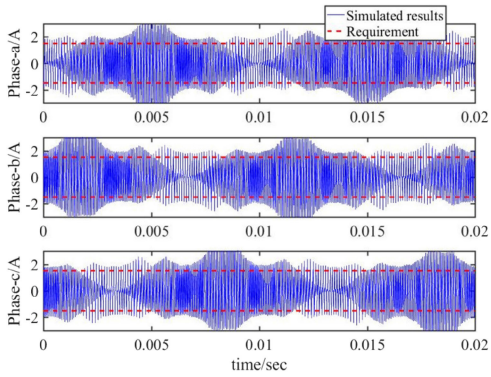

Fig. 13. Current ripple of three phases with T-VSFPWM.

Fig. 11 shows the comparison of current ripple between simulation and prediction for phase-a in different cases. From the zoom-in details of current ripple in several switching cycles for normal SVPWM, it is clear that the current ripple is reset in each switching cycle. Case 1 stands for the predicted peak-to-peak value of current ripple, with a constant inductance (720 μH); In case 2, the varying effective inductance (L_a) is considered to calculate the peak-to-peak value of current ripple, but ignoring the influence of $i_a dL_a/di_a$; case 3 represents the predicted results considering the inductance variation of L_a^* proposed in this paper. By comparing with the simulated current ripple, significant errors can be observed in both cases 1 and 2. Though the effective inductance variation is taken into account in case 2, the prediction error is still significant. Using the artificial inductance L_k^* and the general single-phase model discussed in Section II, the predicted peak-to-peak value of current ripple matches well with the simulated current ripple, which demonstrates the previous current ripple analysis.

B. Modified Variable Switching Frequency PWM

To validate the effectiveness of the proposed M-VSFPWM, extensive simulation studies with wide range of inductance variation in three-phase inductors are carried out. Fig. 12 shows the three-phase current ripple with normal CSFPWM, and the maximum peak-to-peak value is 3 A, which is the control target for both T-VSFPWM and M-VSFPWM. In Fig. 13, the peak-to-peak values of three-phase current ripple exceed the requirement in many switching cycles, thus it is out of control

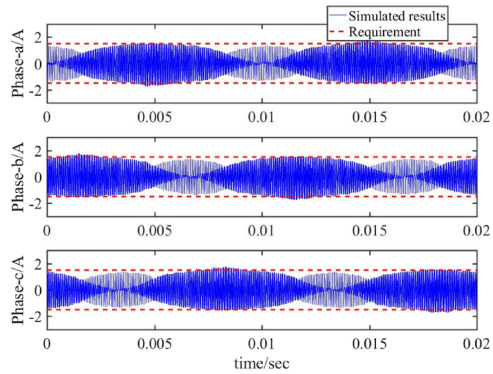

Fig. 14. Current ripple of three phases with M-VSFPWM.

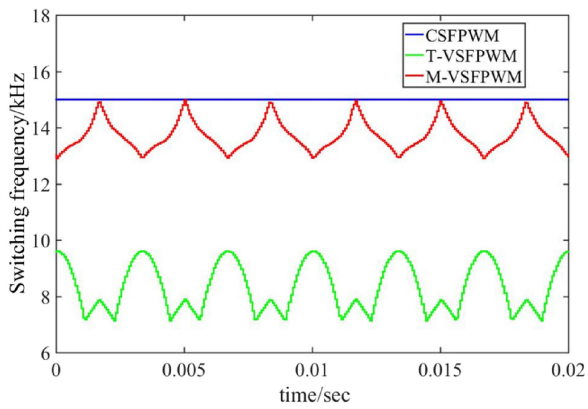

Fig. 15. Switching frequency comparison.

with T-VSFPWM. It is worth noting that the reason why these errors are significant is that the T-VSFPWM does not involve inductance variation in its current prediction model [18]. By contrast, the peak-to-peak value of three-phase current ripple for proposed M-VSFPWM can reach and not beyond the requirement almost in every switching cycle, as shown in Fig. 14. In this case, comparing with the normal CSFPWM, the proposed M-VSFPWM takes up extra computing time in each interruption of DSP, around 9.1 μs.

Fig. 15 shows the comparison of switching frequency. Comparing with the normal CSFPWM whose switching frequency is always a constant (15 kHz), switching frequency of T-VSFPWM varies between 7.1 and 9.6 kHz, but the peak-to-peak value of three-phase current ripple is out of control in this case as can be seen in Fig. 13. It means that the varying switching frequency generated from T-VSFPWM is not accurate for the peak-to-peak value control of three-phase current ripple, under the condition of inductance variation. It should be noted that, in proposed M-VSFPWM, the peak-to-peak value of three-phase current ripple is well controlled within the requirement and the corresponding switching frequency varies between 13 and 15 kHz, resulting in 9.1% average switching frequency reduction. In addition, comparing with the normal CSFPWM, the ac harmonic current for M-VSFPWM gets a wider distribution in frequency-domain as can be seen in Fig. 16, resulting in lower harmonic current peak value.

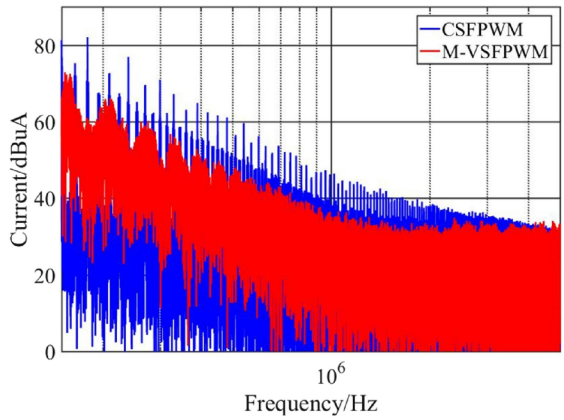

Fig. 16. AC current spectrum comparison.

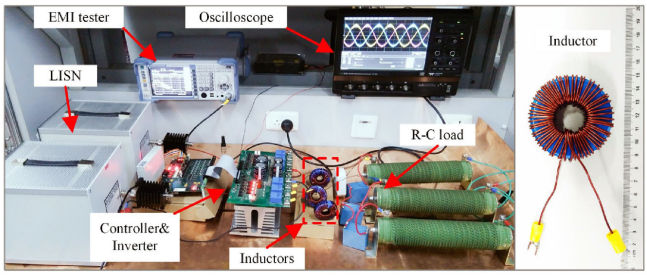

Fig. 17. Picture of experimental setup.

V. Experimental Verification

In order to verify the above analysis, related experiments are carried out in a insulated gate bipolar translators (IGBTs)-based VSI with parameters shown in Table I, and the inverter work condition is the same as the simulation. Inductors are designed with FeSiB core materials and its inductance is designed based on the guideline [23], assuring the required soft saturation. An IPM module named 6MBP20RH060 from Fuji Inc. is connected to *L*–*C* type filters, and the load resistors are connected in "Y" type. The HDO4054 oscilloscope is used to record the phase current, and the harmonics spectrum of phase current is achieved by R&S EMI test receiver. A current probe with the measurement frequency range of 20 Hz–200 MHz is used here to capture the conductive current, and then transfers it to the EMI test receiver through the RF input 50 Ω connector. The physical map of each part of the platform is presented in Fig. 17. In this experiment, the control program is computed based on the DSP of TMS320F28335.

A. Artificial Inductance Measurement and Current Ripple Prediction

Fig. 18 shows the experiment circuit of the effective inductance measurement. The resistance is 5 Ω and the frequency of ac supply is set to 50 Hz, where the impedance of the resistor is much larger than the inductor. Under three-phase ac 75 V supply, both the voltage and current of the inductor are measured, as shown in Fig. 19. It can be seen that the voltage of the inductor is no longer a sinusoidal wave with a sine current because of the inductance saturation. Then the flux linkage can

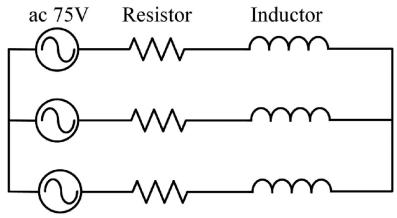

Fig. 18. Experiment circuit of inductance measurement.

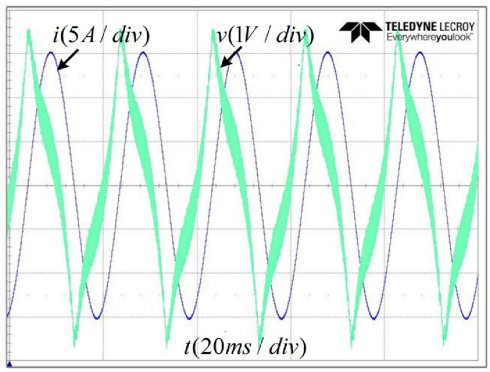

Fig. 19. Measured voltage and current of the inductor.

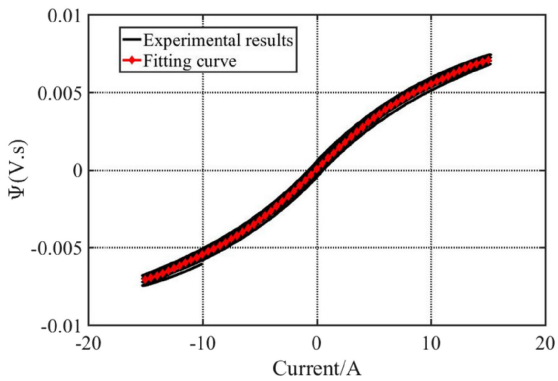

Fig. 20. Flux linkage-current loop.

be achieved with (17). By adjusting the series resistance (R_s) and initial value of flux linkage, the symmetric Ψ–i loop is depicted as shown in Fig. 20. A method of polynomial fitting is adopted to approximate the quantitative expression between the bias current and the effective inductance, and the curve of the inductance versus bias current is finally obtained as shown in Fig. 8. Moreover, the artificial inductance can be further achieved with (3), as shown in Fig. 21. As discussed in Section II, the component of $i_k dL_k di_k$ will facilitate the inductance variation with the increasing current, as shown in Fig. 22. It should be noted that the value of $i_k dL_k di_k$ increases in the range from 11 to 15 A in this case.

$$\Psi(t) = \int_0^t [u(t) - R_s i(t)]dt \tag{17}$$

Fig. 23 shows the experimental current ripple of phase-*a* and the predicted peak value in different cases. It can be clearly seen that when the inductance saturation is neglected in case 1, there will be significant current ripple prediction error from

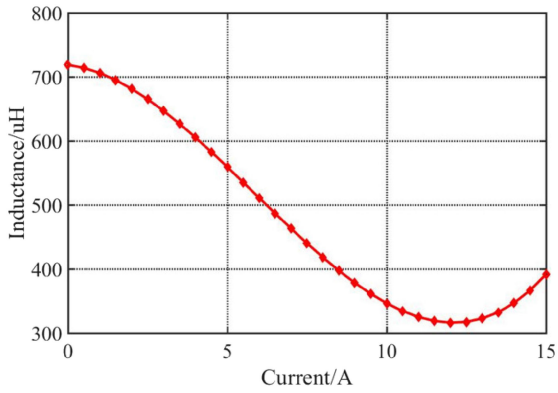

Fig. 21. Artificial inductance with bias current.

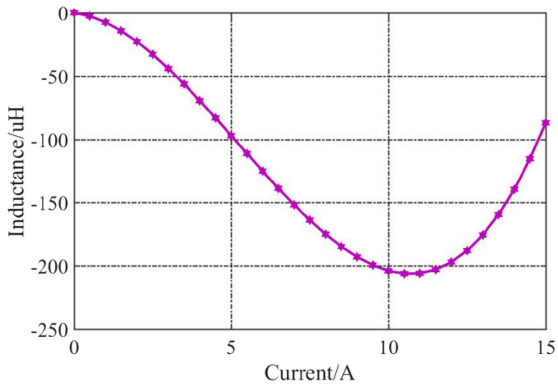

Fig. 22. $i_k dL_k/di_k$ variation with bias current.

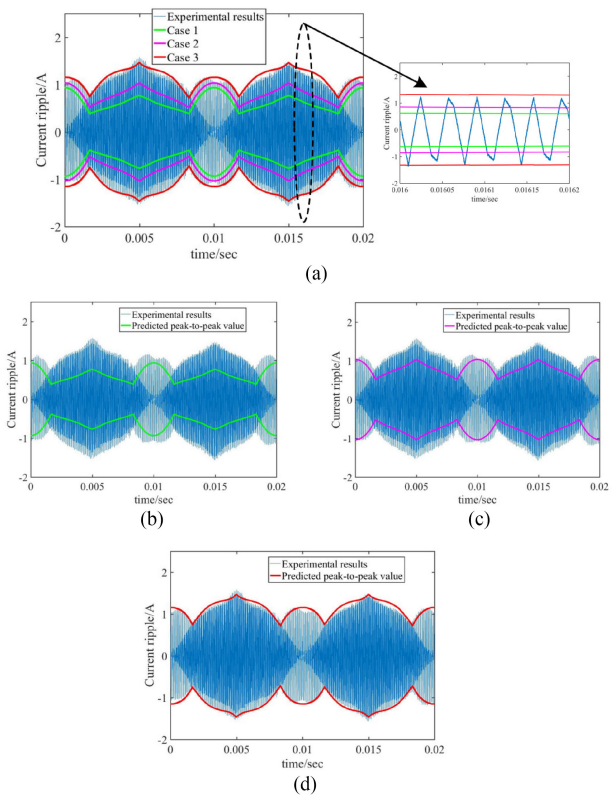

Fig. 23. Experimental results: current ripple comparison of phase-a. (a) General plot. (b) Case 1. (c) Case 2. (d) Case 3.

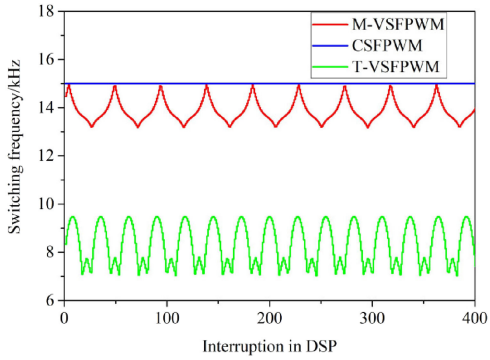

Fig. 24. Switching frequency comparison (experimental results).

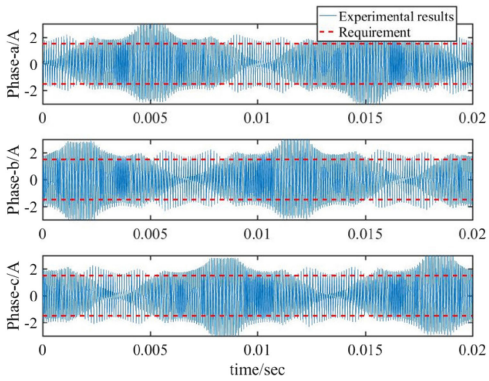

Fig. 25. Current ripple with T-VSFPWM (experimental results).

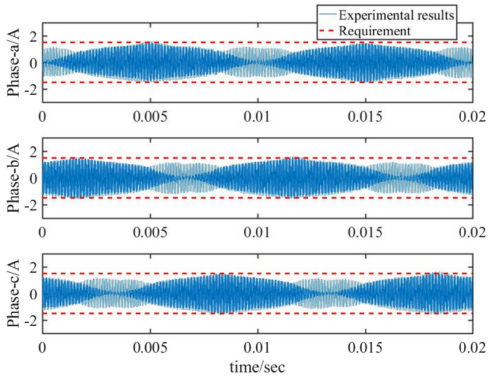

Fig. 26. Current ripple with CSFPWM (experimental results).

the experimental results. In case 2, simply putting a variable effective inductance in the prediction model without considering $i_a dL_a/di_a$ will still cause prediction error. Predicted peak-to-peak value in case 3 matches well with the experimental results, which illustrates the validity of the proposed single-phase model for current ripple calculation.

B. Modified Variable Switching Frequency PWM

In order to see the performance of the variable switching frequency (VSF) technique, some experiments have been carried out with normal CSFPWM, T-VSFPWM, and the proposed M-VSFPWM, with the identical requirement (3 A) of current ripple peak-to-peak value. From Fig. 24, different from the CSFPWM with a constant switching frequency of 15 kHz, the switching frequency of the T-VSFPWM is varying from 7.2 to

TABLE II
COMPARISON BETWEEN CSFPWM AND M-VSFPWM

Method	Current ripple peak-to-peak value (A)	Number of commutations	E_{sw} (A)	THD of inverter side(%)	THD of load side(%)	Loss saving (%)
CSFPWM	3	300	2572.0	6.94	0.79	8.4
M-VSFPWM	3	273	2355.7	7.60	0.79	

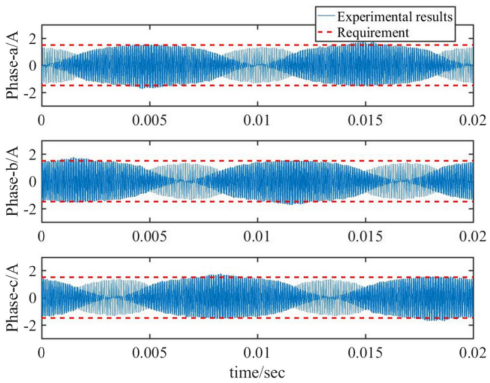

Fig. 27. Current ripple with M-VSFPWM (experimental results).

9.5 kHz, and the variation range for M-VSFPWM is between 13.2 and 15 kHz. Since the inductance used to predict current ripple is always considered as a constant value (720 μH), a much lower average switching frequency is produced by the T-VSFPWM. However, it can be seen from Fig. 25 that the peak-to-peak value of three-phase current ripple for the T-VSFPWM is out of control because of the mistake in output switching frequency, which means that the T-VSFPWM is not suitable for current ripple control under the condition of wide inductance variation. From Figs. 26 and 27, comparing with the CSFPWM, the peak-to-peak value of three-phase current ripple under proposed M-VSFPWM can reach and not beyond the requirement in every switching cycle, which further illustrates the validity of current ripple analysis in Section II. Therefore, the effectiveness of the proposed M-VSFPWM has been demonstrated for current ripple control under the condition of the inductance saturation.

Switching losses are determined by device voltage, switching transition times, the number of commutations, and current value in switching instants [24]. For a two-level VSI, the device voltage is always fixed in dc-link voltage. It is given that the switching transition time is kept to be a constant. A parameter describing the switching losses is defined as (18), and then loss saving can be obtained by (19). From Table II, 8.4% switching losses is reduced with proposed M-VSFPWM in this case. Since there is a tradeoff between average switching frequency and output current quality, the total harmonic distortion (THD) of output current in inverter side gets a little worse with M-VSFPWM. Moreover, Fig. 28 shows the number of commutations and the switching losses saving for different modulation index with M-VSFPWM, where the load resistance is set to 7 Ω.

$$E_{sw} = \sum_{k=1}^{N} |i(t_k)| \tag{18}$$

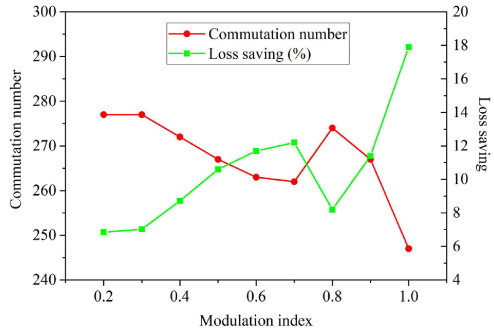

Fig. 28. Switching losses saving and number of commutations in different modulation index.

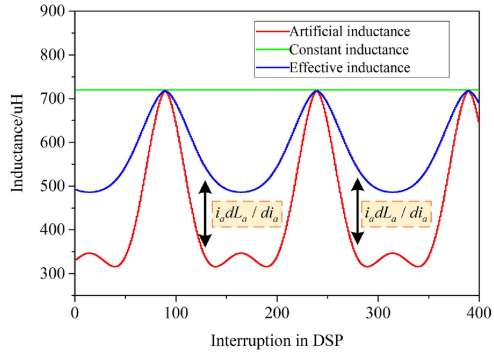

Fig. 29. Updating inductance.

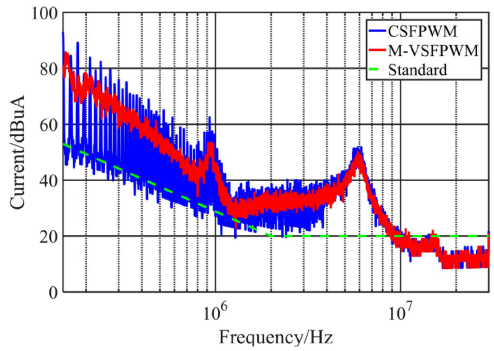

Fig. 30. EMI comparison.

$$\text{Loss saving} = \left(1 - \frac{E_{sw,M-\text{VSFPWM}}}{E_{sw,\text{CSFPWM}}}\right) \cdot 100\% = \left(1 - \frac{\sum_{k=1}^{N1} |i(t_k)|}{\sum_{k=1}^{N2} |i(t_k)|}\right) \cdot 100\% \tag{19}$$

where $i(t_k)$ is the instant current value in the kth commutation and N_1 and N_2 represent the number of commutations per fundamental period.

Fig. 29 shows the updating L_a and L_a^* used for current ripple prediction in each interruption of DSP. In each interruption, the artificial inductance is updated once, and it can be seen that there is a significant inductance difference between the effective inductance and the artificial inductance. Thanks to the switching frequency spreading, M-VSFPWM has a better EMI performance as shown in Fig. 30 with the selected EMI standard. Comparing with the CSFPWM, a reduction of 10 dB can be seen in the 150–900 kHz range with M-VSFPWM.

VI. Conclusion

In this paper, the influence of inductance saturation on the analysis and calculation of current ripple has been studied. The concept of artificial inductance has been introduced to illustrate the inductance variation caused by the saturation of the core materials, which consists of the effective inductance and the term of $i_k dL_k/di_k$. A new CM voltage expression is derived with consideration of inductance variation in three-phase inductors. A general single-phase model considering inductance saturation has been derived and used to predict current ripple in real time. It has been proved that in order to predict current ripple precisely, artificial inductance model is needed which is more than just simply putting the varying effective inductance in the prediction model.

VSFPWM has been proposed for three-phase VSIs in previous literatures, but it has not been developed to consider the inductance saturation for current ripple control. This paper has tried to propose an M-VSFPWM method to control the current ripple when the output inductor is with a wide range of inductance variation. The proposed M-VSFPWM has been compared with the CSFPWM and the T-VSFPWM, including the current ripple peak-to-peak value, switching losses, and EMI performance. With the proposed M-VSFPWM, both the switching losses and EMI can be improved and the effective control of current ripple is realized simultaneously. The theory and results presented show that the inductance saturation plays an important role in current ripple analysis and should be considered for VSFPWM design.

References

[1] V. Blasko, "Analysis of a hybrid PWM based on modified space-vector and triangle-comparison methods," *IEEE Trans. Ind. Appl.*, vol. 33, no. 3, pp. 756–764, May/Jun. 1997.

[2] K. Zhou and D. Wang, "Relationship between space-vector modulation and three-phase carrier-based PWM: A comprehensive analysis [three-phase inverters]," *IEEE Trans. Ind. Electron.*, vol. 49, no. 1, pp. 186–196, Feb. 2002.

[3] G. D. Holmes and T. A. Lipo, *Pulse Width Modulation for Power Converters—Principles and Practice (IEEE Press Series on Power Engineering)*. Piscataway, NJ, USA: Wiley, 2003.

[4] D. Boroyevich, X. Zhang, H. Bishinoi, P. Mattavelli, and F. Wang, "Conducted EMI and systems integration," in *Proc. 8th Int. Conf. Integr. Power Electron. Syst.*, Nuremberg, Germany, 2014, pp. 1–14.

[5] K. Raggl, T. Nussbaumer, and J. W. Kolar, "Guideline for a simplified differential-mode EMI filter design," *IEEE Trans. Ind. Electron.*, vol. 57, no. 3, pp. 1031–1040, Mar. 2010.

[6] W. C. Lo, C. C. Chan, Z. Q. Zhu, L. Xu, D. Howe, and K. T. Chau, "Acoustic noise radiated by PWM-controlled induction machine drives," *IEEE Trans. Ind. Electron.*, vol. 47, no. 4, pp. 880–889, Aug. 2000.

[7] A. Ruiz-Gonzalez, F. Vargas-Merino, J. R. Heredia-Larrubia, M. J. Meco-Gutierrez, and F. Perez-Hidalgo, "Application of slope PWM strategies to reduce acoustic noise radiated by inverter-fed induction motors," *IEEE Trans. Ind. Electron.*, vol. 60, no. 7, pp. 2555–2563, Jul. 2013.

[8] X. Mao, R. Ayyanar, and H. K. Krishnamurthy, "Optimal variable switching frequency scheme for reducing switching losses in single-phase inverters based on time-domain ripple analysis," *IEEE Trans. Power Electron.*, vol. 24, no. 4, pp. 991–1001, Apr. 2009.

[9] D. Jiang and F. Wang, "Current-ripple prediction for three-phase PWM converters," *IEEE Trans. Ind. Appl.*, vol. 50, no. 1, pp. 531–538, Jan. 2014.

[10] D. Jiang and F. Wang, "A general current ripple prediction method for the multiphase voltage source converter," *IEEE Trans. Power Electron.*, vol. 29, no. 6, pp. 2643–2648, Jun. 2014.

[11] G. Grandi, J. Loncarski, and C. Rossi, "Comparison of peak-to-peak current ripple amplitude in multiphase PWM voltage source inverters," in *Proc. 15th Conf. Power Electron. Appl.*, Lille, France, Sep. 3–5, 2013, pp. 1–10.

[12] G. Grandi, J. Loncarski, and O. Dordevic, "Analysis and comparison of peak-to-peak current ripple in two-level and multilevel PWM inverters," *IEEE Trans. Ind. Electron.*, vol. 62, no. 5, pp. 2721–2730, May 2015.

[13] F. Yang, A. R. Taylor, H. Bai, B. Cheng, and A. A. Khan, "Using d–q transformation to vary the switching frequency for interior permanent magnet synchronous motor drive systems," *IEEE Trans. Transp. Electrific.*, vol. 1, no. 3, pp. 277–286, Oct. 2015.

[14] S. Jayalath, D. Ongayo, and M. Hanif, "Modelling powder core inductors for passive filters in inverters using finite element analysis," *Electron. Lett.*, vol. 53, pp. 179–181, Feb. 2017.

[15] K. Lu, X. Lei, and F. Blaabjerg, "Artificial inductance concept to compensate nonlinear inductance effects in the back-EMF-based sensorless control method for PMSM," *IEEE Trans. Energy Convers.*, vol. 28, no. 3, pp. 593–600, Sep. 2013.

[16] T. Zou, X. Han, D. Jiang, R. Qu, and D. Li, "Inductance evaluation and sensorless control of a concentrated winding PM vernier machine," *IEEE Trans. Ind. Appl.*, vol. 54, no. 3, pp. 2175–2184, May. 2018.

[17] Q. Wei, B. Liu, and S. Duan, "Current ripple analysis and controller design for grid-connected converters considering the soft saturation nature of the powder cores," *IEEE Trans. Power Electron.*, vol. 33, no. 10, pp. 8827–8837, Oct. 2018.

[18] D. Jiang and F. Wang, "Variable switching frequency PWM for three phase converters based on current ripple prediction," *IEEE Trans. Power Electron.*, vol. 28, no. 11, pp. 4951–4961, Nov. 2013.

[19] S. Bhattacharya, S. K. Sharma, D. Mascarella, and G. Joós, "Sub-fundamental cycle switching frequency variation based on output current ripple analysis of a three-level inverter," *IEEE J. Emerg. Sel. Topics Power Electron.*, vol. 5, no. 4, pp. 1797–1806, Dec. 2017.

[20] Y. Zhang and H. Yang, "Generalized two-vector-based model-predictive torque control of induction motor drives," *IEEE Trans. Power Electron.*, vol. 30, no. 7, pp. 3818–3829, Jul. 2015.

[21] Y. Zhang, H. Yang, and B. Xia, "Model predictive torque control of induction motor drives with reduced torque ripple," *IET Elect. Power Appl.*, vol. 9, no. 9, pp. 595–604, Feb. 2015.

[22] D. Jiang, Q. Li, and Z. Shen, "Model predictive PWM for AC motor drives," *IET Elect. Power Appl.*, vol. 11, no. 5, pp. 815–822, May. 2017.

[23] Adv. Technol. & Mater. Co., Ltd., Beijing, China. *Magnetics*. [Online]. Available:http://www.atmcn.com/cpyfw/cpdh/fjnmjdc/fjnmjfm/cifenxin/2015/1227/3171.html

[24] O. O˜nederra, I. Kortabarria, I. Mart´ınez de Alegr´ıa, J. Andreu, and J. Ignacio G´arate, "Three phase VSI optimal switching loss reduction using variable switching frequency," *IEEE Trans. Power Electron.*, vol. 32, no. 8, pp. 6570–6576, Aug. 2017.

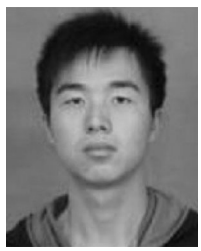

Qiao Li received the B.S. degree from the School of Electrical and Electronic Engineering, Huazhong University of Science and Technology, Wuhan, China, in 2015. He is currently working toward the Ph.D. degree in electrical engineering at Huazhong University of Science and Technology.

His research interests include pulsewidth modulation strategy, converter control, and power hardware-in-the-loop.

Dong Jiang (S'05–M'12–SM'16) received the B.S. and M.S. degrees in electrical engineering from Tsinghua University, Beijing, China, in 2005 and 2007, respectively. He received the Ph.D. degree in power electronics and motor drives from the University of Tennessee, Knoxville, TN, USA, in Dec. 2011.

He was with United Technologies Research Center, Connecticut, USA, as a Senior Research Scientist/Engineer from 2012 to 2015. He has been with Huazhong University of Science and Technology, Wuhan, China, as a Professor since July 2015. He has authored or coauthored more than 80 IEEE journal and conference papers. His research interests include power electronics and motor drives.

Dr. Jiang was the recipient of three Prize Paper awards in IEEE conferences. He is an Associate Editor of IEEE TRANSACTIONS ON INDUSTRY APPLICATIONS.

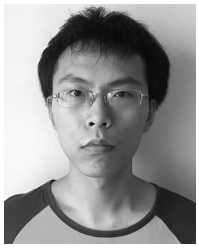

Yechi Zhang received the B.S. degree in electrical engineering from North China Electric Power University, Beijing, China, in 2014. He is currently working toward the Ph.D. degree in electrical engineering at Huazhong University of Science and Technology, Wuhan, China.

His research interests include EMI/electromagnetic compatibility in power converters and EMI filter design.